Astronomy & Astrophysics

The dynamics of the solar chromosphere: comparison of model predictions with millimeter-interferometer observations

M. Loukitcheva[1,2], S. K. Solanki[1], and S. White[3]

[1] Max-Planck-Institut für Sonnensystemforschung, 37191 Katlenburg-Lindau, Germany
   e-mail: marija@peterlink.ru
[2] Astronomical Institute, St. Petersburg University, 198504 St. Petersburg, Russia
[3] Astronomy Department, University of Maryland, College Park, MD 20742, USA

ABSTRACT

We analyze the millimeter intensity spectrum expected from the dynamic model of Carlsson & Stein together with the interferometric observations of the quiet Sun obtained at a wavelength of 3.5 mm with the Berkeley-Illinois-Maryland Array. The observational data products (Fourier and wavelet spectra, brightness histograms) are compared with the corresponding products obtained for the Carlsson & Stein (CS) models. We estimate how the limited spatial resolution of the observations influences the comparison with the predictions of chromospheric dynamic models and discuss the limitations of a one-dimensional non-magnetic modeling approach. In addition, we test the effect of the integration time of the BIMA observations on the dynamic signatures. The dependence of the observed brightness variations on spatial resolution is studied by employing artificial image degradation and approximating the obtained dependence by power laws. We are able to establish a correspondence between the CS model predictions and the observational data under assumptions on the horizontal coherence length of the oscillations. The reconstructed brightness rms values indicate that, assuming the coherence length of oscillating elements to be of order of 1″, the oscillation power in the observations recorded with 10″ resolution agrees within a factor of 2 with the power predicted by the CS model. We argue that millimeter continuum observations promise to be an important diagnostic of chromospheric structure and dynamics. Based on the analysis carried out in this work, the appropriate wavelengths to look for dynamic signatures are in the range 0.8−5.0 mm. Further millimeter interferometric observations with longer sequences and higher spatial resolution are highly desirable along with the development of realistic three-dimensional radiation magnetohydrodynamic simulations.

Key words. Sun: chromosphere – Sun: oscillations – Sun: radio radiation

1. Introduction

This is the second in a series of papers that explore the nature of the solar chromosphere by means of interferometric observations in the millimeter wavelength range. In the previous contribution (White et al. 2006, hereafter called Paper I) we presented the first high-resolution two-dimensional maps of the solar chromosphere made with an interferometric array at millimeter wavelengths and used the data to investigate spatially-resolved power spectra of features within the solar atmosphere. While the dynamic state of the solar chromosphere is now well established through observations made at different wavelengths stretching from the EUV (Carlsson et al. 1997; Judge et al. 2001; Krijger et al. 2001, etc.) via the visible (Cram & Damé 1983; Rutten & Uitenbroek 1991; Lites et al. 1993) to the far IR (e.g. Kopp et al. 1992), the results of Paper I have led to the extension of the wavelength range of significant chromospheric dynamics detection to millimeter wavelengths as well.

Radiation hydrodynamic simulations of Carlsson & Stein (1992, 1995, 1997, 2002a, hereafter CS) have explained the most prominent observational signature of chromospheric dynamics, the formation of Ca II K and H grains, by upward propagating acoustic waves and the interactions between the shocks they produce in the middle chromosphere. According to their dynamic model the chromospheric gas is mostly in a cool state. In this picture the hot chromospheric gas is in a transient state and the dynamics determine the very nature of the chromosphere. The alternative picture is that propagated by various families of static, plane parallel models (e.g. Vernazza et al. 1981; Fontenla et al. 1993), which exhibit a permanent chromospheric temperature rise. The dynamics are a secondary phenomenon in this picture and may be considered to be a perturbation of the static structure.

The observations do not as yet allow us to distinguish between these radically different scenarios for the structure and dynamics of the chromosphere (e.g. Solanki 2004). In particular, the commonly used atomic spectral lines are sensitive mainly to the warmer gas and exhibit only a relatively small fluctuation in brightness, although the temperature in the model shows large excursions (Carlsson & Stein 1995).

Loukitcheva et al. (2004a) proposed a new diagnostic that may be able to select between these two types of models, namely high resolution time series of submillimeter and millimeter continua. It was demonstrated that spatially and temporally resolved observations should clearly exhibit the signatures of the strong shock waves found in the CS models, if these are present in the true quiet Sun. The analysis of the radio emission expected from the CS model simulation revealed that dynamic effects drastically alter the height at which the dominant contributions

to emission occur. As a result, the brightness temperatures are extremely time-dependent at millimeter wavelengths, following changes in the atmospheric parameters. Waves with a period of approximately 180 s are seen in the resulting model brightness temperature as a function of time.

Unfortunately, radio data from the literature cannot distinguish between the models. The existing data are either single-dish time sequences with low spatial resolution or larger-field images with poor time resolution. To compare the models with such data, we can average spectra from the CS simulations. The results agree with the existing millimeter data despite the absence of a temperature rise at low chromospheric heights in the model. However, reasonable agreement was also found between observations and the static FAL models. The major shortcoming of the currently available radio observations is their low spatial and temporal resolution which allows only spatially averaged characteristics to be deduced and is insufficient to resolve oscillations. For this reason, they do not effectively discriminate between competing models.

In this paper we use observational data obtained at 3.5 mm with the Berkeley-Illinois-Maryland Array (BIMA), which with 10 antennas provides the best instantaneous imaging at this wavelength among currently available instruments. The limitations of the MEM deconvolution technique used to create snapshots and time-series analysis of the brightness variations at 3.5 mm in the BIMA data within these limitations have been described in Paper I. We reported on significant oscillations with brightness variations of $50-150$ K found in all observed solar features in the frequency range $1.5-8$ mHz. The intensity oscillations appeared to be wave trains of finite duration lasting typically for $1-3$ wave periods. Though there is a possibility that oscillating power from regions of weak flux is redistributed across the image we believe that we are able to distinguish between the properties of network and cell interiors and between bright and less bright parts of active regions. The statistical analysis done in Paper I revealed a tendency toward short period oscillations in the quiet Sun and longer periods in the active region. The same difference in behavior was exhibited by internetwork and network regions in the quiet Sun, with the latter having a tendency for longer period oscillations, but it needs to be confirmed by further studies.

In this paper we concentrate on a comparison of the data products (Fourier and wavelet spectra, etc.) with the corresponding products obtained for the CS model. Most of the effort of the work described in this paper has gone into analysing the CS models and into trying to estimate how the finite spatial (and to a lesser extent temporal) resolution of the observations may influence the results. In addition we address the limitations resulting from interpreting the observations within the context of a one dimensional and non-magnetic atmospheric model. A preliminary version of some of the results may be found in Loukitcheva et al. (2004b).

The paper is structured as follows. In Sect. 2 we give a brief description of the CS model-based millimeter spectrum, of the observational data, as well as of the applied analysis techniques. In Sect. 3 we present the results of the time-series analysis of the model radio spectra and of the observed brightness variations. In Sect. 4 we discuss the influence of finite spatial and temporal resolution and consequences thereof for the comparison between the model and observations. Finally, some qualitative consequences of a full three dimensional model treatment with a magnetic field included and a summary of the obtained results are given in Sect. 5.

2. Model and data

2.1. The CS model and model millimeter spectrum

Carlsson & Stein (1992, 1995, 1997, 2002a) have developed a self-consistent radiation-hydrodynamic model of the solar chromosphere. The one-dimensional equations of mass, momentum, energy and charge conservation were solved simultaneously and implicitly together with the non-LTE radiative transfer of hydrogen, calcium and helium spectra. Continuum radiation from other elements was treated as a background continuum in LTE. The calculations were done on an adaptive mesh to ensure stability in the presence of shocks. The authors included the effects of non-equilibrium ionization, excitation and radiative energy exchange from several atomic species on fluid motions, and the effect of motions on the emitted radiation. Their initial atmosphere is in radiative equilibrium above the convection zone without line blanketing and extends 500 km into the convection zone. It includes a corona and a transition region, through setting the upper boundary at a height of 10 Mm to a temperature of 10^6 K. Incident radiation from the corona causes ionization in the helium continua in the upper chromosphere and a slow temperature rise above a height of 1 Mm. After the start of the simulations waves are driven through the atmosphere by a subphotospheric piston with the velocity taken from an hour long series of Doppler measurements in a photospheric Fe I line. Propagating waves increase in amplitude and form shocks above a height of 1 Mm. High-amplitude shocks producing temperature differences in excess of 10^4 K may originate when shocks merge due to the difference in propagation speed. As a consequence, the kinetic temperature significantly exceeds the initial values only episodically during short time intervals, while the mean structure of the dynamic atmosphere has a temperature of about 5000 K throughout most of the chromosphere, in contrast to standard empirical models (such as the FAL models), which manifest a temperature increase from a minimum value at about 500 km above $\tau(500 \text{ nm}) = 1$. The simulations do not include a magnetic field and thus are confined to represent regions without a strong magnetic field, like the quiet Sun internetwork.

Loukitcheva et al. (2004a) computed radio brightness temperatures from the dynamic simulations of Carlsson and Stein and, after averaging over time, compared them with the spatially averaged observed brightness temperatures T_b of the quiet Sun from single-dish observations at submillimeter and millimeter wavelengths. The time series of atmospheres produced by the CS dynamic simulation used for that analysis covered 18 wave periods of approximately 180 s each, with a cadence of 10 s between the snapshots. Two wave periods with 2 s cadence were examined in greater detail. The submillimeter and millimeter emission at 24 selected wavelengths in the range $0.05-20$ mm, emerging from the dynamic models, was computed under the assumption that radio continuum radiation for wavelengths shorter than 3 centimeters is formed due to the opacity contributed by thermal bremsstrahlung. In Fig. 1a we show the excess intensity (brightness temperature) as a function of wavelength and time. The excess brightness temperature is the brightness temperature of a snapshot minus the time averaged brightness temperature. A negative grey scale is chosen, so that black represents the brightest events. In Figs. 1b, 1c and 1d we plot light curves at the wavelengths 0.1 mm, 3.4 mm and 10 mm, which we analyze further in greater detail. The plot is similar to Fig. 3 of Loukitcheva et al. (2004a), but here we plot individual light curves for a different set of wavelengths.

Wave periods of approximately 180 s can be clearly distinguished in the intensity at all considered wavelengths. Striking
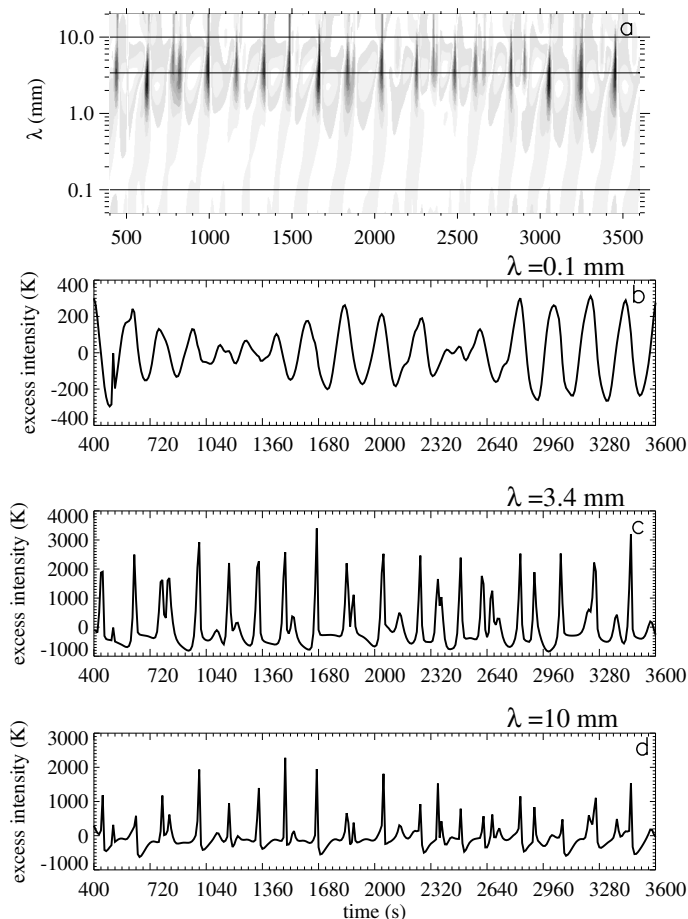
Fig. 1. Evolution of the model millimeter spectrum with time. Plotted is the excess spectrum, i.e. the instantaneous spectrum from which the time-averaged spectrum has been subtracted. **a)** Negative grey scale representing excess intensity as a function of time and wavelength. Thin solid lines mark the position of λ = 0.1 mm, 3.4 mm and 10 mm. **b)–d)** Excess intensity at the wavelengths 0.1 mm, 3.4 mm and 10.0 mm, respectively, vs. time. The first 400 s of the simulation are not considered.

is the difference from one period of time to another. Time intervals which show extremely high excess intensity, such as the period t = 500−680 s, are usually characterized by the presence of merging shocks. There are also periods of time which exhibit little excess intensity (see the interval t = 2300−2480 s in Fig. 1). At sub-mm wavelengths (Fig. 1b) the excess intensity evolution is similar in shape to harmonic waves. Towards longer wavelengths the peaks in brightness become narrower and also higher (Fig. 1c), while at the longest wavelengths (Fig. 1d) most fluctuations in brightness are small, with interspersed short and intense brightenings. The differences in the light curves at the 3 wavelengths investigated are caused primarily by the difference in the formation heights of the emitted radiation. The model millimeter spectrum is discussed further in Sect. 3.

2.2. The BIMA observations at 3.5 mm

We discuss observational results based on the images of the Sun made interferometrically at a wavelength of 3.5 mm with the Berkeley-Illinois-Maryland Array (BIMA), which has the largest number of dishes of any existing millimeter interferometer and is the telescope best suited for such observations. BIMA is a 10-element interferometric array consisting of 6.1 m

diameter dishes. The data analyzed were obtained on August 31, 2003 with 6 BIMA antennae. The interferometer was in its most compact ("D") configuration for these observations, providing a nominal spatial resolution of order 10″ (within a 2′ field of view), but minimizing the effects of atmospheric phase distortions on the data. The images were deconvolved using a maximum entropy method (MEM) and restored with a Gaussian beam. The final images were 128 pixels square, with a cell size of 3″. All images were corrected for the primary beam response and truncated in a 72″ radius field of view. Fifteen second cadence was used to make the image snapshots, which resulted in 3 successive data cubes for the observed target in the quiet Sun region, each 30 min long. We refer the reader to Paper I for the details of the interferometric image restoration, including description of the limitations imposed by the MEM deconvolution and the extensive tests of BIMA sensitivity to oscillation detection. In Paper I each observed field was divided into internetwork (IN), network (NW) and an intermediate region based on masks constructed from the BBSO Ca II K images and time-averaged radio images for each data set. Here we use a more stringent criterion to allocate spatial pixels to the internetwork. We consider only those times series obtained by applying the original internetwork masks to belong to the IN if in addition they exhibit maximum Fourier power in the 3-min range (120−240 s). By this restriction we hope to account for 2 different phenomena: firstly, to discard the pixels classified to represent the internetwork by the original criterion but that may contain a significant admixture of signal from nearby network elements because of inadequate spatial resolution; secondly, to prevent the examination of the pixels with a significant leakage of longer period oscillation power due to the using of the MEM deconvolution for creating snapshots. We thus hope to select pixels exhibiting a behaviour typical of the internetwork.

2.3. Analysis technique

The model and observational data were analyzed by a variety of means. These include a Fourier analysis, which consists of applying the Fast Fourier Transform algorithm, including a 10% cosine apodisation, and forming the power spectrum. The confidence levels for the model data were derived by considering the global wavelet spectrum as a measure of the background spectrum, against which peaks were tested. For the observed time series the long-term evolution (with typical periods exceeding 10 min) at each spatial pixel was removed by subtracting a third order polynomial fit to the series before processing. This compensates for drifts, evolution and partly for horizontal motions such that features move into or out of a given pixel. The statistical significance of the observed oscillations was estimated using the prescription of Groth (1975) under the assumption that the actual noise present in the data is white. Only power above the 99% confidence level was considered to be significant and was used further for statistical studies.

The duration of the oscillations, as well as the evolution of their periods, were studied by means of a wavelet analysis. We used the complex valued Morlet wavelet as a mother wavelet. For the wavenumber k, which describes the number of oscillations within the wavelet itself, we employ k = 6, the smallest wavenumber that satisfies the admissibility condition and allows an accurate signal reconstruction. Significance levels of 99% were calculated assuming the global wavelet spectrum as a background spectrum, following Torrence & Compo (1998). The statistically significant oscillations derived from the Fourier power spectra under the assumption of white noise and

from the wavelet power spectra using global wavelet spectra were found to be similar. We take this result as a validation of the noise model employed (white noise). Finally, we consider only observed time series showing brightness variations exceeding the noise level, which corresponds to 100 K in brightness temperature. We also determine rms (root-mean-square) values and study histograms of the brightness. More details on the analysis techniques are given in Paper I.

3. Results

3.1. Analysis of the model millimeter spectrum

Here we present the results of Fourier and wavelet analyses of the spectral time series computed by Loukitcheva et al. (2004a) on the basis of the CS dynamic model. In Fig. 2a we show the Fourier power as a function of period and frequency, with black representing highest power. At each wavelength the Fourier power is normalized to the highest power peak. Three $\lambda - t$ cuts of the grey scale plot at $\lambda = 0.1$ mm, 3.4 mm and 10 mm are marked in Fig. 2a and the corresponding power spectra, normalized to the total power at each wavelength, are shown in Figs. 2b, 2c and 2d.

At sub mm – short mm wavelengths (see Fig. 2b) the dominant power peak is at a frequency of 5 mHz (corresponding to a period of 200 s), with smaller peaks at 5.75 mHz (period of 175 s) and 4.2 mHz (period of 240 s). The peak at 5 mHz decreases in amplitude with increasing wavelength. At 3.4 mm (Fig. 2c) it is still present but maximum power is found at a frequency of 5.75 mHz. From Figs. 2c and 2d it is seen that at long mm wavelengths the main peak starts to decrease slightly in power relative to the total power (actually, the peak at 5.75 mHz has roughly the same fraction of the total power – within a factor of 2 – at all wavelengths). For wavelengths longer than 3 mm significant power is found at high frequencies, i.e. periods shorter than 100 s (frequencies above 10 mHz), and at low frequencies, i.e. periods greater than 250 s (see Fig. 2a). The source of the additional power at very high and low periods is the steepening of the 3-min waves into shocks as they propagate up into less dense gas. This steepening is also seen in Fig. 1. At short wavelengths, which sample gas at a level close to the traditional temperature minimum, the oscillations are almost sinusoidal and are consequently well represented by a single frequency. At longer wavelengths, which sample, on average, higher layers in the atmosphere, the oscillations have been distorted in the sense that individual peaks in the radio brightness times series become sharper and less sinusoidal (see Fig. 1) due to the increasing temperature contrast and the steepening of the waves into shocks. A sharper peak needs a larger number of frequencies to be well described in Fourier space. A periodic succession of sharp peaks in time results in a single sharp Fourier power peak, as well as a background of power at other frequencies, similar to the power spectra in Figs. 2c and 2d. Most striking is the significant power at high frequencies above 8.5 mHz. We should note that no evidence of high frequency oscillations exceeding the noise level was found in the BIMA light curves analyzed in this work (e.g., see Fig. 5). Some of the simulated power outside the 5.5–6.5 mHz frequency range may result from the fact that not all shocks propagate at the same speed. While the train of waves is quite regular in the lower part of the model atmosphere (sampled by short mm wavelengths), some shocks catch up with others and even merge in the upper chromosphere, making the spacing more irregular (see Fig. 1).
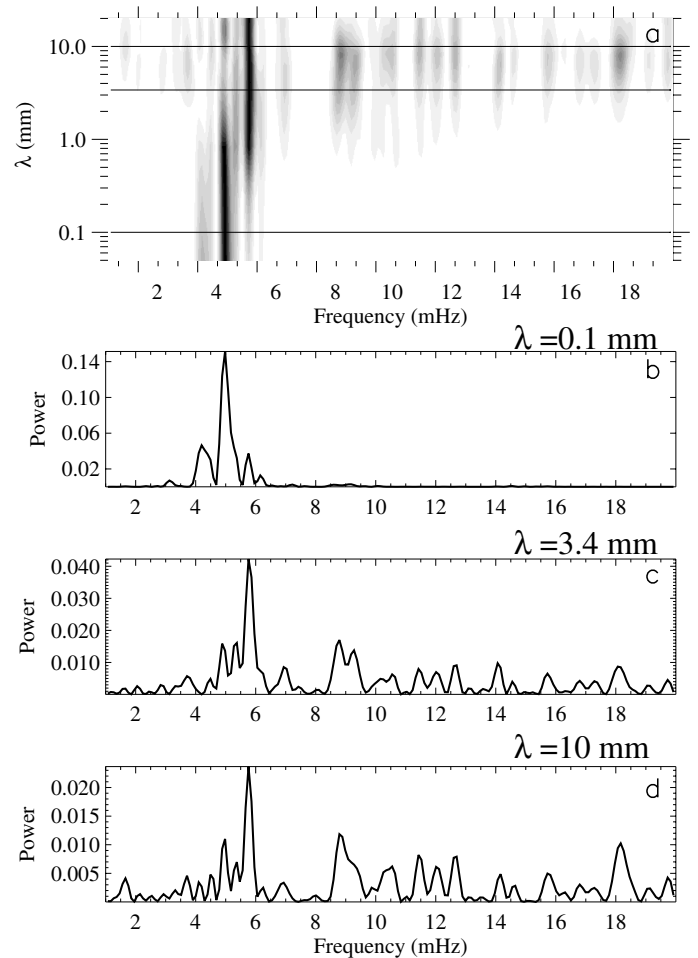

Fig. 2. Millimeter wave intensity power spectrum due to the CS model. **a)** Fourier power as a function of period and wavelength. Darker signifies higher power. The grey scale has been normalized such that the highest power is black at each wavelength. Thin solid lines mark $\lambda = 0.1$ mm, 3.4 mm and 10 mm. **b)–d)** The Fourier power spectra at the wavelengths 0.1 mm, 3.4 mm and 10 mm, respectively. The power is normalized to the total (integrated) power at each wavelength.

A careful look at Fig. 1 reveals a time delay between the oscillations at long and short millimeter wavelengths. By considering the times when individual brightness peaks occur at 3 selected wavelengths we determined these time lags to be 21 s between the oscillations at 0.1 mm and 3.4 mm, 23 s between 0.1 mm and 10 mm (brightness variations at short mm wavelengths lead the ones at longer wavelengths) and no measurable lag between 3.4 and 10 mm. Hence, it is possible to distinguish between standing and propagating waves by comparing sub-mm with mm observations, but not if only millimeter observations are available.

Wavelet power spectra at the 3 selected wavelengths are shown in Fig. 3. The darker shaded regions show the location of higher wavelet power. Cross-hatched regions indicate the cone of influence (COI), where edge effects become important (see Torrence & Compo 1998). The plots allow us to judge how constant the wave amplitude and period remain over time. They reveal significant differences between the 3 considered wavelengths. At 0.1 mm significant power is present in a broad range of frequencies during the whole time series. However, maximum power is found close to a period of 200 s (frequency of 5 mHz) at almost all times (and the maximum power is 100 times higher
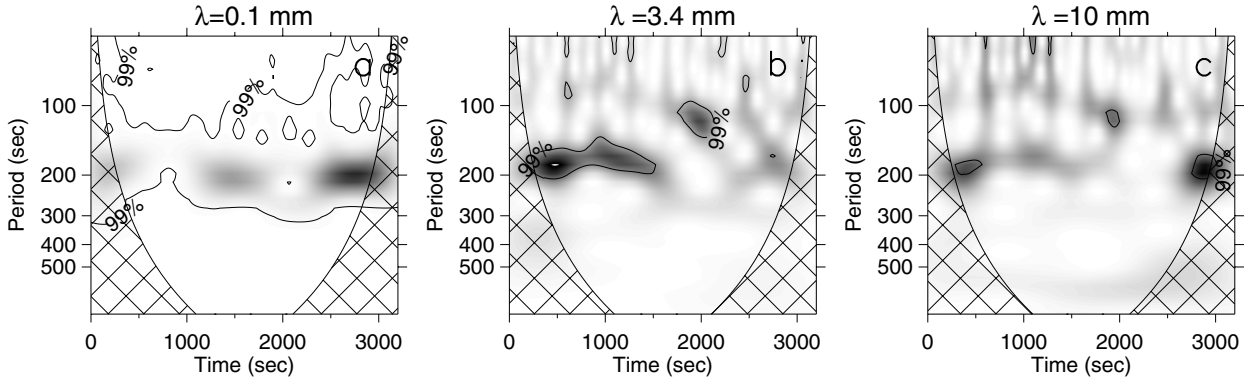
Fig. 3. Wavelet power spectra as a function of time and period of the output of the CS model for $\lambda = 0.1$ mm, 3.4 mm and 10 mm (grey scale). Cross-hatched regions indicate the cone of influence, where the nearby boundary affects the reliability of the results. Black solid lines represent the 99% significance level of oscillations assuming the global wavelet spectrum as a background spectrum. The grey scale is chosen such that darker shading signifies higher power.
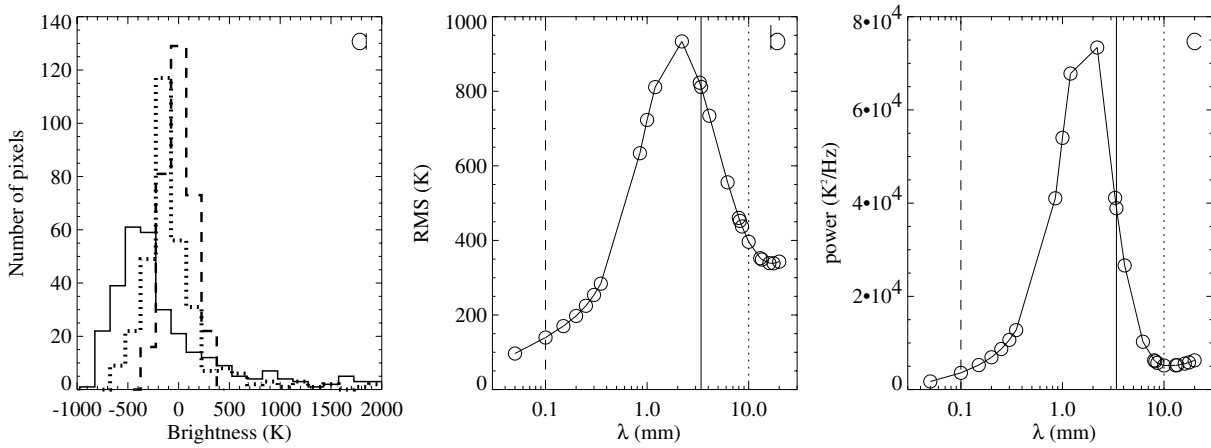

Fig. 4. Characteristics of the millimeter spectrum expected from the CS model. **a)** Histograms of the model brightness for $\lambda = 0.1$ mm, 3.4 mm and 10 mm, represented by dashed, solid and dotted lines, respectively. **b)** The rms brightness temperature as a function of wavelength. **c)** The dominant peak power of the CS model spectral time series as a function of wavelength. Thin vertical lines mark the location of the 3 analysed wavelengths.

than the 99% confidence level). Also, there are 3 time intervals of enhanced power, lasting for about 600 s each. At 3.4 mm the wavelet power at any given time is confined to a narrow range of periods and the maximum power lies only at twice the 99% significance level, i.e. the wavelet power is less significant than at 0.1 mm at all times. During the first half of the run maximum power is reached around 180 s (frequency of 5.6 mHz), while later there is also significant power at $100-150$ s, although it is of short duration (about 300 s) and there are multiple significant very short duration peaks at periods below 100 s. This figure shows that the Fourier peak at around 115 s (8.7 mHz) in Fig. 2c is most probably due to a shock that is catching up with a slower earlier shock. This interpretation is confirmed by Fig. 1, where at $t = 2400$ s from the start of the simulations ($t = 2000$ s from the start of the analyzed time series) one can distinguish a brightness peak merging with a very close secondary peak, both being out of phase with the main 3-min period. For $\lambda \geq 10$ mm the model time series demonstrates power in the 3-min range, but it is significant only at the beginning and at the end of the run with a duration comparable with the COI size for the corresponding period. The peak power is further reduced at 10 mm, being only 1.27 times the 99% significance level. The significant peak at a period close to 115 s at 2000 s after the start of the series is also seen at the longest wavelength, implying that the 115 s peak in Fig. 2d has the same origin as in Fig. 2c.

Next, we analyze amplitude statistics of the fluctuations of the model millimeter intensity with time by plotting intensity histograms at each wavelength ($\lambda = 0.1$ mm, 3.4 mm and 10 mm) in Fig. 4a, represented by dashed, solid and dotted lines, respectively. At 0.1 mm the histogram is rather symmetric, with a skewness, which denotes the degree of asymmetry of a distribution, of only 0.17 and an rms of the brightness temperature of 140 K. At 10 mm the rms value is higher, at 396 K, while the skewness of the histogram remains small, being only 0.14. The intensity distribution at 3.4 mm demonstrates considerable width and asymmetry, producing the highest rms of 812 K and the highest skewness of 2.72.

The shape of the histograms in Fig. 4a can, again, be understood by comparing with the time series in Fig. 1. The quasi-sinusoidal fluctuations seen at 0.1 mm produce a nearly symmetric histogram. At 3.4 mm the asymmetry in the signal is evident, with strong excursions to high intensities, which are not compensated by corresponding excursions to low intensities. At 10 mm at first sight the situation is similar to that of 3.4 mm, i.e. very asymmetric intensity excursions. However, a closer look reveals that most of the time the intensity fluctuates around an average value and the fluctuations to larger values are of very short duration. This gives rise to a histogram that is nearly symmetric with a long, but very low tail stretching to high intensity values.
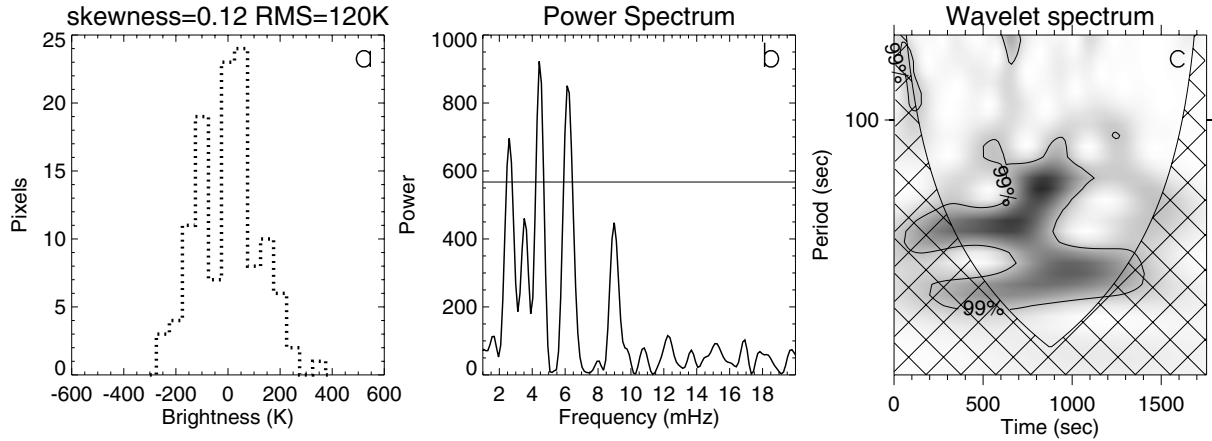
Fig. 5. Oscillations at the internetwork location ($-245''$, $-107''$) from the QS4 dataset. **a)** The histogram of observed brightness. **b)** Fourier power spectrum as a function of frequency. **c)** Wavelet power spectrum as a function of time and period (grey scale). Cross-hatched regions indicate the cone of influence, where the nearby boundary affects the reliability of the results. Thin solid lines in **b)** and **c)** represent the 99% significance level of oscillations.

The rms brightness temperature as a function of wavelength is depicted in Fig. 4b, together with the thin lines marking the location of the 3 analysed wavelengths. In Fig. 4c we plot the power of the dominant Fourier peak as a function of wavelength. Both the rms and the power of the peak grow significantly with increasing wavelength. After the maximum values are reached at 2.2 mm, they decrease equally rapidly towards longer wavelengths. At longer wavelengths the power in the peak drops more rapidly with wavelength than the rms amplitude. The reason can be found in Fig. 2c, where in addition to the dominant peak one can distinguish a pronounced background of power at multiple frequencies at long wavelengths. Figures 4b and 4c can be used to identify 0.8−5.0 mm as the appropriate range of mm wavelengths at which one can expect the clearest signatures of dynamic effects. The BIMA observations lie within this range. Judging purely from the histograms the most robust signature of shock waves is expected at around 2.2 mm, where not only the broadest, but also the most strongly skewed histograms are seen. The amplitude of oscillations is expected to be up to 15% of the quiet-Sun brightness temperature which is of order 6000 K at 2.2 mm according to Loukitcheva et al. (2004a). However, none of the existing millimeter arrays operates at this wavelength.

3.2. Analysis of the observed brightness at 3.5 mm

As mentioned in Sect. 2.1 the output of the CS simulations is best compared with observations referring to regions with weak magnetic field like the quiet Sun internetwork. However, even there a magnetic canopy may be present, which could affect some of the results (Jones & Giovanelli 1982; Solanki & Steiner 1990; Bianda et al. 2002). Indeed, recent studies based on data recorded with the SUMER instrument on board SOHO (e.g., Carlsson & Stein 2002b; Karlsen & Carlsson 2002; Wilhelm & Kalkofen 2003) have demonstrated that magnetic effects can not be omitted even in the internetwork areas. The results reported by the above authors suggest that a basic intensity level in the quiet Sun internetwork is set by a magnetic heating process with superimposed intensity variation caused by acoustic waves, with the latter being successfully depicted by the CS simulations.

In Paper I we showed that the observed power spectra of internetwork pixels exhibit significant power at multiple frequencies, typically in the 3−5 min period range, but also at longer periods of 7−10 min. As an illustration, in Fig. 5 we plot the Fourier power spectrum and wavelet spectrum together with the brightness histogram for the internetwork location ($-245''$, $-107''$) from the QS4 dataset. The significant power peaks of the Fourier spectrum are at 4.5 mHz (corresponding to a period of 220 s), 6 mHz (167 s) and 2.5 mHz (400 s). The wavelet spectrum shows similar periodicities, which differ in duration. The oscillations in the 150−200 s period range last for only 2 frequency cycles, while the power at 250 s is present during the first half of the time series. At the period of 400 s the oscillations are detected over the whole time interval. The corresponding brightness histogram, depicted in Fig. 5a, is nearly symmetric (with a skewness of 0.12). The rms of the brightness temperature is 120 K. Both values are small relative to those predicted by the CS model (~800 K and 2.7 for rms and skewness, respectively). Another difference is the absence of longer periods in the model power spectrum (Figs. 2 and 3b). Statistical fluctuations may affect this result, since the observed time series is rather short. Indeed, the observed time series at individual pixels reveal different brightness distributions. Therefore, it is more robust to compare average properties of many spatial pixels of the data.

After averaging over pixels, representing supergranule cell interiors, we obtain a relatively symmetric histogram with a skewness of 0.16, shown in Fig. 6a. The rms of the intensity underlying this histogram is 95 K, which is similar to that of the single time series shown in Fig. 5. The differences between computed and observed rms values and histogram skewness remain. For comparison we plot in Fig. 6b the histogram of the observed brightness for all locations representing the network from 3 QS data cubes. The average network histogram exhibits a higher rms value of 130 K and a skewness of 0.18. Hence the network elements are not only brighter, they also show larger fluctuations.

4. Discussion

The discrepancies between model predictions and observational results found in Sect. 3 do not as yet rule out the CS models, since the direct comparison of the oscillations predicted by model and observed variations is inappropriate. The model is one dimensional and hence does not predict a coherence length of the oscillations. This quantity plays a central role for the
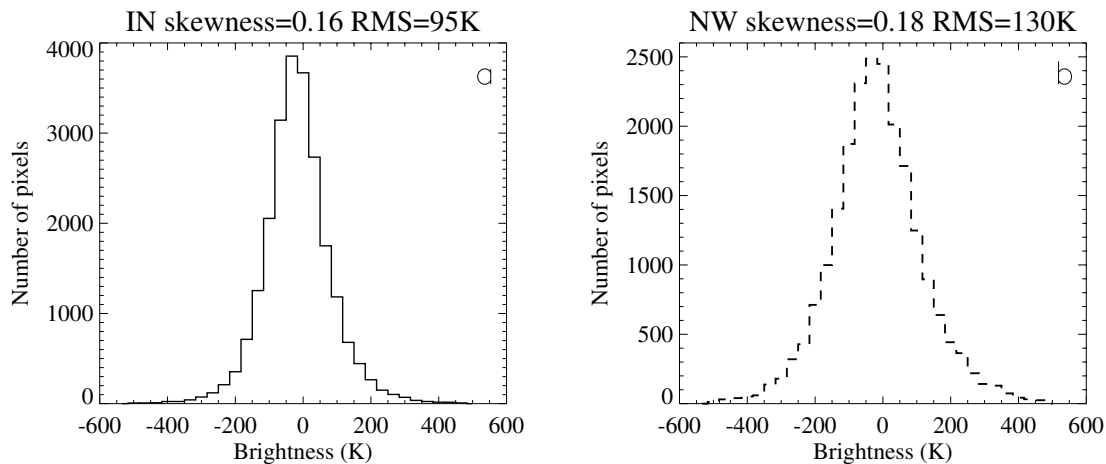
Fig. 6. Histograms of the observed brightness for all locations representing **a)** the internetwork and **b)** the network.
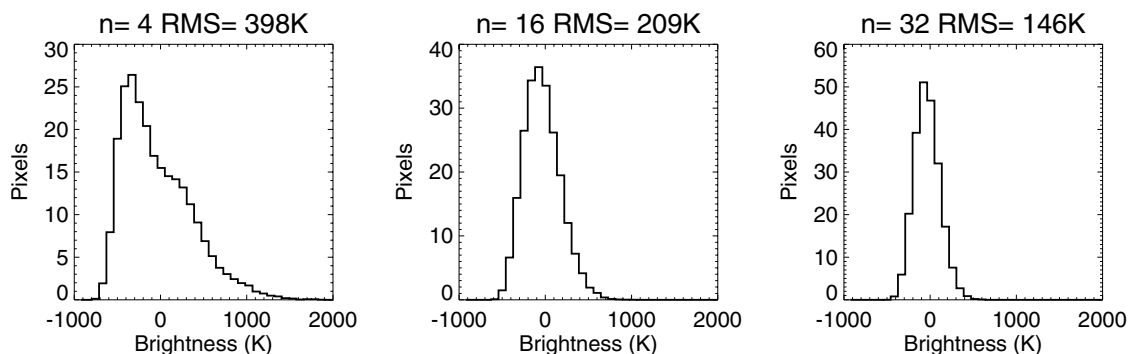
Fig. 7. Results from Monte Carlo simulations illustrating the effect of an increasing amount of spectral smearing on the histogram. Plotted are averages over $n = 4, 16, 32$ model time series with random phase shifts (*from left to right*).

comparison between model and data. It is expected to be smaller than the $10''$ spatial resolution of the observations. In the further analysis we focus on the search for appropriate methods to compare the model and observations. To this end we test the effects of limited resolution applied to the model predictions and to the observations. Additionally, in Sect. 5 we discuss the limitations imposed by the interpretation of the observations in the context of a one dimensional and unmagnetized model and qualitatively discuss some consequences of going to a 3D and magnetized model of the solar chromosphere.

### 4.1. The effect of finite spatial resolution: model

Since we have no spatial information in the model we assume the following simple scenario to describe the effect of finite spatial resolution on the data products. Consider a situation in which many internetwork sources, distributed more or less randomly on the solar surface inject waves of similar amplitude and periods but random phases into the chromosphere. The measured signal when integrating spatially over all these sources is a superposition of all the incoherent waves from these sources. We therefore model the effect of limited spatial resolution on the model predictions by averaging together millimeter wavelength intensity resulting from the CS model with random phase shifts. In particular, we take the time series computed by Loukitcheva et al. (2004a) for $\lambda = 3.4$ mm, shift it by a random amount of time (shorter than 1/3 of the time series) and add it to the unshifted time series. In this way we have averaged over $n = 2, 4, 8, 16, 32$ randomly shifted time series. For each n we have

performed Monte Carlo simulations with 100 test runs and derived the histogram, power spectrum and wavelet spectrum.

In Fig. 7 we present the results obtained for 3 selected cases. Most striking is the effect of wave mixing on the form of the intensity distribution. With increasing n the histogram becomes more symmetric and narrower (the skewness decreases from 0.91 for $n = 4$ to 0.34 for $n = 32$), thus getting closer to the observed distribution. The rms brightness temperature also decreases with increasing n, producing an rms value of 147 K for $n = 32$, which is similar to the observed value. The effect of the wave mixing on the Fourier power spectrum is not significant, except for a general decrease in power $\sim 1/n$.

It is well known that in the network power at periods of $400-800$ s is strong (e.g. Lites et al. 1993). Such periods are indeed seen almost everywhere in the BIMA data. In Paper I we had argued that these longer periods are introduced by the admixture of some signal from the network into the internetwork. To include this observational effect into the models we have added a sinusoidal component, corresponding to longer periods (typical of the network), to the mixed time series. The amplitude and the period of the sinusoid were randomly chosen from the amplitude range of $100-300$ K and periods in the range of $400-800$ s.

Histograms, power spectra and wavelet spectra, resulting from a second set of Monte Carlo simulations, are plotted in Fig. 8 for the numbers of averaged time series $n = 2, 8, 16$. With an added sinusoidal component the rms amplitudes decrease more rapidly with n. The histogram becomes nearly symmetric with a skewness of 0.24 already for $n = 16$. As expected, the additional network component changes the
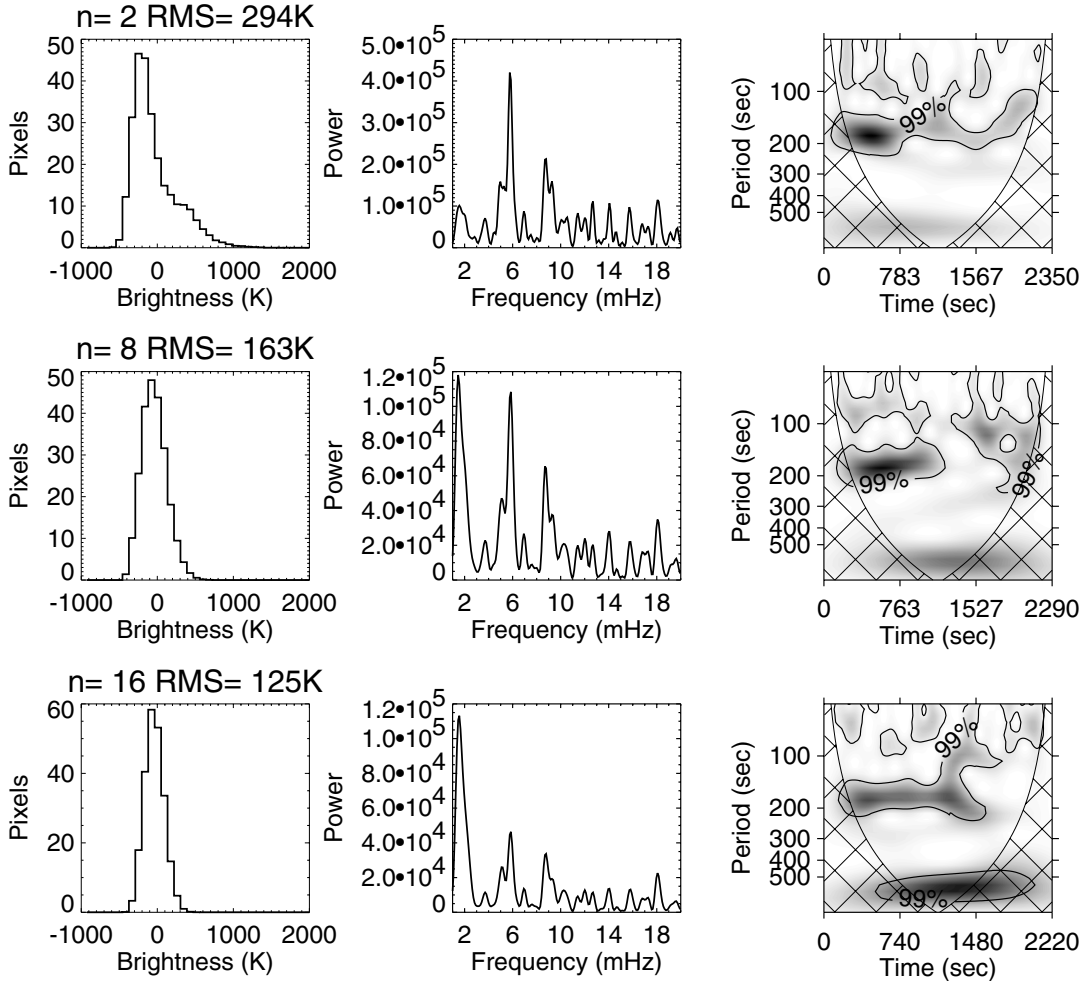
Fig. 8. The same as Fig. 7 for averages over $n = 2, 8, 16$ model time series with random phase shifts combined with a sinusoidal component (*top to bottom*). In addition to the histogram (*left*), now also the Fourier power spectrum (*middle*) and wavelet spectrum (*right*) are plotted.

distribution of the Fourier and wavelet power as well. Thus, the peak at about 2 mHz gets more of the total power with increasing n. Hence, while for $n = 2$ the power maximum is at 5.75 mHz, for $n = 8$ and 16 the maximum shifts to 1.75 mHz.

As a result, we are able to obtain reasonable agreement in the rms values, histogram skewness, power and wavelet spectra between the millimeter oscillations predicted by the CS model and observed brightness variations when modeling the effect of limited spatial resolution by mixing several model time series and adding a sinusoidal component. In spite of this success we cannot say that the model predictions are confirmed by the observations, however, since we have no guarantee that $n = 16$ is an appropriate number of waves to mix in order to represent a typical observed internetwork element. If the oscillating sources cover about 50% of the whole area (Carlsson et al. 1997), for a circular beam of $10''$ $n = 16$ corresponds to sources located on average $1.5''-2''$ apart. This distance corresponds roughly to the average size of granules. Hence, $n = 16$ would be appropriate if every or every second granule emitted independent 3-min oscillations. Before discussing this further we describe two further tests, that were carried out.

4.2. The influence of finite temporal resolution: model

The integration time of the observations should affect the signal amplitude, in particular the sharp brightness peaks, seen in

Figs. 1c and 1d. We now study the effect of time integration on the model radio intensity at the 3 selected wavelengths for the time interval $t = 500-680$ s (see Fig. 1), which was sampled in the simulations at a cadence of 2 s. The original time series were "smeared" in time using running averages over different time intervals between 6 s and 30 s. The resulting smeared radio brightness light curves for 3.4 mm are represented by dotted lines in Fig. 9a, while the original brightness from the model is depicted by the solid line. The brightness of the peak, plotted in Fig. 9b as a function of integration time (triangles), decreases by up to 30% of its original value for an integration time of 15 s, which was employed in the BIMA observations under consideration. The corresponding rms brightness temperature (squares in Fig. 9b) decreases by up to 10% of its original value. At shorter wavelengths the dependence on integration time is not pronounced, while at 10 mm the integration time drastically affects the intensity variations. The brightness peak decreases significantly in amplitude (by up to 75% of its original value for an integration time of 30 s) and becomes more broad with increasing time integration. The rms value of the brightness temperature at 10 mm decreases to nearly half of its value.

4.3. The influence of finite spatial resolution: observations

Here we carry out an analysis complementary to that in Sect. 4.1 and spatially smear the observational data further. We then use
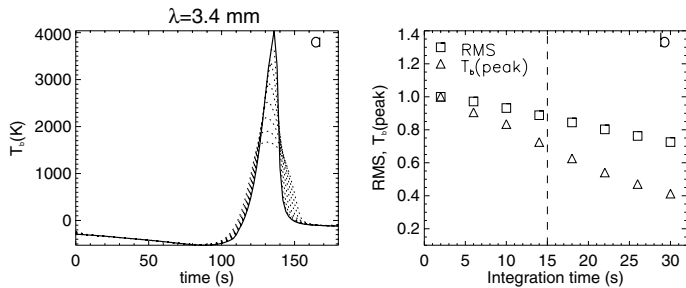
Fig. 9. The influence of integration time on model intensity at $\lambda = 3.4$ mm. **a)** The original brightness extracted from the CS model for the time span $t = 500-680$ s (solid line) and estimated brightness variations (dotted lines) for integration times of $6-30$ s. **b)** The ratio of the rms brightness temperature to its value in the original model as a function of integration time (squares). The same for the brightness of the peak (triangles). The dashed vertical line marks the integration time of the BIMA observations.
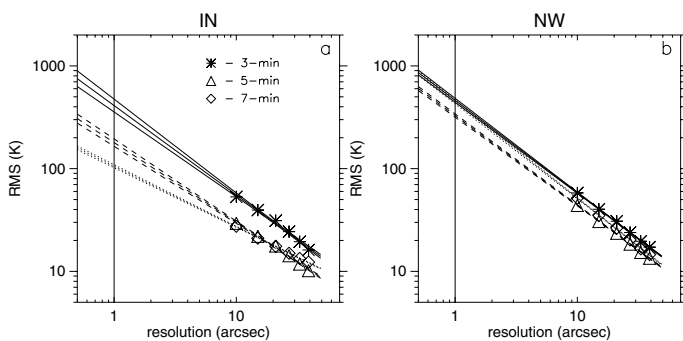
Fig. 10. The observed rms amplitude of the brightness variations in 3 frequency ranges as a function of spatial resolution, depicted on a logarithmic scale, for **a)** internetwork locations from 3 QS data sets with maximum Fourier power in the range of 3 min and **b)** network locations from 3 QS data sets. The 3-min, 5-min and 7-min amplitudes are represented by star, triangle and diamond symbols, respectively. The power law fits to the data (thicker central lines) with 1σ error bars (narrower outer lines) are indicated by solid, dashed and dotted lines for the rms in 3-min, 5-min and 7-min frequency ranges, respectively. Vertical dotted lines mark $1''$ spatial resolution.

the resulting dependence of the rms on the smearing to extrapolate to high spatial resolution in order to obtain a very rough estimate of the expected average rms. Such extrapolated values can, within limits, also be compared with the original simulations. To test the dependence of the rms in different frequency ranges on spatial resolution we have degraded the observational data by taking averages over 3×3, 5×5, ..., 15×15 pixels, each $3''$ across. We calculated the rms amplitudes for the degraded time series averaged separately over the regions representing internetwork and network. The rms of the individual frequencies was reconstructed from the wavelet power spectra, following Torrence & Compo (1998). We show the results obtained for the internetwork and network in Fig. 10, where we plot the rms amplitude as a function of the size of the resolution element in 3 frequency ranges on a logarithmic scale. The stars, triangles and diamonds depict the rms in 3-min ($120-249$ s), 5-min ($250-399$ s) and 7-min ($400-1000$ s) frequency ranges, respectively. The extrapolation to higher resolution was done by approximating the dependence of rms on spatial resolution by power laws, which are shown in Fig. 10 by solid, dashed and dotted lines. We also show the error bars at the 1σ level for the fitted power laws, which are plotted with the same line type as the fitted curves.

Hofmann & Deubner (1995) presented an analysis of the rms amplitude of p-mode oscillations as a function of spatial resolution for different heights in the solar atmosphere. They obtained values of the exponents of a power law fit in the range between -0.56 (He I 10830 Å) and -0.77 (Ca II 8542 Å). The exponents of the fitted power laws derived in this work for all locations without separation into internetwork and network at 3.5 mm are -0.74, -0.77 and -0.73 for the 3-min, 5-min and 7-min ranges, respectively, in good agreement with the results of Hofmann & Deubner (1995). Of interest is that the power law exponents deduced for the internetwork emission are smaller than the exponents obtained from the network pixels (see Table 1). The higher network exponents as compared to the internetwork values (in particular for the 7-min range) are in agreement with the idea that network oscillations are confined to localized small structures.

The estimated rms amplitudes at $1''$ resolution of the full time series and in the 3 frequency ranges for internetwork and network are listed in Table 1. This choice of spatial scale is supported by the estimate given at the end of Sect. 4.1 and by 3-dimensional radiation-hydrodynamic simulations of Wedemeyer et al. (2004) (see Sect. 5). To check the reconstructed rms in different frequency ranges we calculated total brightness variations of the averaged time series as a function of spatial resolution. The results for the total rms are listed in columns marked "all" in Table 1. For the internetwork emission the expected amplitude of oscillations at a spatial resolution of $1''$ is about 600 K. The rms amplitude estimated from the CS model millimeter spectrum has a similar value ($\sim$800 K for the wavelength of 3.4 mm). Thus, by extrapolation of the observed oscillations to $1''$ size of the resolution element we obtain a reasonable agreement between the CS model products and the observations.

In the bottom part of Table 1 we list the estimated rms in a particular frequency interval relative to the total rms. This ratio reflects the contribution from a specific frequency range to the total rms as a function of spatial resolution. As expected, for the cell interiors the relative rms in the 3-min frequency range decreases with decreasing resolution. This result is in agreement with the generally accepted view that with decreasing spatial resolution multiple patches of coherent waves are averaged together and 3-min internetwork power is smeared out. In the case of the 7 min oscillations the relative rms amplitude increases with decreasing resolution. This supports our interpretation that the long periods (7-min range) present in many IN pixels have been introduced by the presence of network fragments within the $10''$ beam centered on the IN region in question. Taken together, it explains the high power of long period oscillations present in the observational internetwork emission and verifies the inadequacy of the available spatial resolution of $10''$ to resolve internetwork elements. For the network elements the ratio of the rms stays mostly constant, with a tendency for the relative rms in the 7-min range to decrease with decreasing resolution, while in the 3-min and 5-min frequency intervals the relative rms amplitude slightly increases. This behavior is in good agreement with the interpretation given above.

5. Summary and conclusions

We have analysed the millimeter intensity spectrum expected from the dynamic model of Carlsson and Stein together with the interferometric observations of the quiet Sun obtained at a wavelength of 3.5 mm with the Berkeley-Illinois-Maryland

Table 1. Exponents of the fitted power laws and rms amplitudes (absolute and relative values), in 3 frequency ranges and in total, observed at 10″ resolution and expected at 1″ resolution for internetwork (IN) and network (NW). By relative rms we denote the rms in a particular frequency interval relative to the rms determined over all frequencies.

	IN				NW			
Absolute rms	3-min	5-min	7-min	all	3-min	5-min	7-min	all
power law exponent	−0.87	−0.78	−0.59	−0.79	−0.90	−0.87	−0.94	−0.90
rms(10″), K	56	30	27	103	58	44	52	133
rms(1″), K	411	179	106	632	462	329	446	1066
$1\sigma(1″)$, K	59	15	4	61	21	12	19	45
Relative rms								
power law exponent	−0.07	0.01	0.20	−	0.03	0.03	−0.05	−
ratio at 10″	0.54	0.29	0.26	−	0.44	0.33	0.39	−
ratio at 1″	0.65	0.28	0.17	−	0.43	0.31	0.42	−

Array. Keeping in mind the limitations of the maximum entropy deconvolution, used to reconstruct observed radio brightness distribution, we confine the observational data analysis to the spatially-resolved time series exhibiting a behaviour typical of the internetwork with the maximum of the Fourier power in the 3-min range. A direct comparison of the model predictions with the observations exhibits large differences. In particular, the rms of the brightness temperature is nearly an order of magnitude larger in the model than in the observations. Since we are not able to resolve individual oscillating elements due to the limited spatial resolution, the direct comparison with the models is not straightforward and an adequate description of the influence of limited spatial resolution is needed. We have taken two different approaches to estimate the influence of the spatial smearing on the parameters of chromospheric dynamics.

In the first approach the effect of limited spatial resolution was modelled by mixing model time series with random phase shifts and adding a sinusoidal component to account for network oscillations which are not present in the model. We demonstrated that for a statistical combination of 16 sources of 3-min oscillations and 1 long-period source we are able to obtain reasonable agreement in the rms values, histogram skewness, Fourier power and wavelet spectra between the observed millimeter oscillations and those predicted by the CS model. We also tested the effect of the integration time of observations. For the BIMA observations the effect is found to be small. At longer wavelengths an integration time larger than 5−10 s can lead to a strong reduction of the brightness temperature fluctuations.

Finally, we investigated the effect of limited spatial resolution on the observed power of the oscillations in the frequency ranges of 3 min, 5 min and 7 min and longer. We confirmed that the spatial resolution of the observations of 10″ hinders a clean separation between cells and network and typically both network and internetwork areas contribute to the recorded radiation. By degrading the resolution further, fitting the dependence of the rms on the spatial resolution by a power law and using this power law to extrapolate the rms of brightness temperature to high spatial resolution values it was found that power in all frequency ranges increases significantly with improving resolution. The reconstructed rms brightness indicates that, assuming the coherence length of oscillating elements to be on the order of 1″, the oscillation power in the observations recorded with 10″ resolution is consistent within a factor of 2 with the power predicted from the CS model and the 3D model of Wedemeyer et al. (2004). There is a hint that the amplitude of the solar oscillations is somewhat smaller than in the models, in agreement with Wilhelm & Kalkofen (2003).

A major limitation of the present work is introduced by the fact that the CS models are one-dimensional and it is not straightforward to compare their output with observations having a limited spatial resolution. This limitation is overcome if the output of a 3-dimensional radiation-hydrodynamic simulation is analysed. This has been done by Wedemeyer-Böhm et al. (2005a), who computed the millimeter wave signature resulting from the simulations of Wedemeyer et al. (2004). These, however, suffer from the fact that the radiative transfer of energy is entirely in LTE, which becomes a poor assumption at chromospheric heights. Also, these simulations do not include a magnetic field. Nevertheless, some of the basic features seen in the 3D model would be representative of the non-magnetic internetwork regions of the solar chromosphere.

These simulations display a complex 3D structure of the chromospheric layers, which is highly dynamical and intermittent on spatial scales comparable to solar granulation and on temporal scales of typically 20−25 s. The chromospheric temperature structure is characterised by a pattern of hot shock waves, which originate from convective motions, and cool gas lying between the shocks.

The comparison of the amplitudes of the temperature fluctuations and the mean temperature in the one-dimensional CS model chromosphere and that of Wedemeyer et al. (2004), is not straightforward as these quantities are strongly influenced by the treatment of radiative transfer, which is different for the two models under consideration. Nevertheless, simply due to the additional spatial dimensions one can expect less variability in the temperature fluctuations and more effective dynamic cooling of regions traversed by a strong shock wave in 3D than in 1D.

The 3-dimensional simulation predicts the coherence length of oscillations to be similar to the size of a solar granule. Thus it supports our assumption of an approximately 1″ size for the appropriate oscillation coherence length scale used in Sect. 4.3 for comparison of the observations with the 1D model. However, in the simulations there is also evidence of wave trains that span larger horizontal scales (Wedemeyer-Böhm, priv. comm.). The analysis of the millimeter wave signatures resulting from the 3D simulations done by Wedemeyer-Böhm et al. (2005a, b) gives an average intensity oscillation contrast at a wavelength of 3 mm of about 24%, which decreases drastically with spatial resolution, leading to a 10% contrast for a resolution of 1″.

At some height in the chromosphere the magnetic field starts dominating the plasma (leading to $\beta \leq 1$; β is defined as the ratio of the gas pressure over the magnetic pressure) and magnetic effects cannot be ignored. The $\beta = 1$ surface, which is often referred to as the "magnetic transition region", lies at a height between 500 km and 2000 km. In this layer different MHD wave modes undergo complicated interactions including mode conversion and coupling, refraction and reflection.

For 3D configurations complex patterns of wave interactions of high variability in both time and space will arise. Thus, the simplified 3D MHD simulations reported by Carlsson & Stein (2002b) have demonstrated that even for a simple photospheric wave field a complex magnetic field geometry creates a complicated wave pattern.

Numerical simulations of MHD wave propagation in a two-dimensional stratified magneto-atmosphere, carried out by Bogdan et al. (2003), have shown that the character of the fluctuations observed in the atmosphere depends considerably on the relative location and orientation of the magnetic canopy with respect to the wave source and the layer at which a diagnostic emission is formed. Thus, for a highly tilted magnetic field, which is meant to represent the internetwork close to a network element, the simulations of Bogdan et al. (2003) show significant reflection in the magnetic canopy layer, with most of the transmitted energy, reduced by radiative losses, in the form of magnetic fast waves traveling at the Alfven speed. Finally, longer period waves can propagate into the chromosphere along tilted field lines than in the field-free atmosphere (De Pontieu & Erdelyi 2004). Hence, at least some magnetic network elements can support lower frequency waves in chromospheric layers. By adding various MHD modes, the inclusion of a magnetic field washes out the clear picture of acoustic 3-min shock waves and reduces considerably the dynamic signatures expected from the latter.

The results of this paper strengthen the conclusions of Paper I regarding the need for further millimeter interferometric observations with longer sequences and higher spatial resolution, which are a promising diagnostic of chromospheric structure and dynamics. Particularly exciting are the prospects of observing with ALMA, which will provide a spatial resolution in the range $0.015''$ to $1.4''$ depending on the configuration (Bastian 2002). According to the analysis carried out in this work, the appropriate wavelengths to look for dynamic signatures are in the range $0.8-5.0$ mm. ALMA will be able to observe at a wavelength of 2.2 mm where the CS model predicts that the largest observable effects will be seen. The development of realistic three-dimensional radiation magnetohydrodynamic simulations is also highly desirable.

References

Bastian, T. S. 2002, Astron. Nachr., 323, 271
Bianda, M., Stenflo, J. O., & Solanki, S. K. 1998, A&A, 337, 565
Bogdan, T. J., Carlsson, M., Hansteen, V. H., et al. 2003, ApJ, 599, 626
Carlsson, M., & Stein, R. F. 1992, ApJ, 397, L59
Carlsson, M., & Stein, R. F. 1995, ApJ, 440, L29
Carlsson, M., & Stein, R. F. 1997, ApJ, 481, 500
Carlsson, M., & Stein, R. F. 2002a, ApJ, 572, 626
Carlsson, M., & Stein, R. F. 2002b, in SOLMAG 2002, Proc. of the Magnetic Coupling of the Solar Atmosphere Euroconference and IAU Coll. 188, ed. H. Sawaya-Lacoste, Noordwijk, Netherlands, ESA SP-505, 293
Carlsson, M., Judge, P. G., & Wilhelm, K. 1997, ApJ, 486, L63
Cram, L. E., & Damé, L. 1983, ApJ, 272, 355
De Pontieu, B., Erdelyi, R. J., & Stewart, P. 2004, Nature, 430, 536
Fontenla, J. M., Avrett, E. H., & Loeser, R. 1993, ApJ, 406, 319
Hofmann, J., & Deubner, F.-L. 1995, A&AS, 113, 583
Groth, E. J. 1975, ApJS, 29, 285
Jones, H. P., & Giovanelli, R. G. 1982, Sol. Phys., 79, 247
Judge, P. G., Tarbell, T. D., & Wilhelm, K. 2001, ApJ, 554, 424
Karlsen, N., Carlsson, M., & Wilhelm, K. 2002, in From Solar Min to Max: Half a Solar Cycle with SOHO, Proc. of the SOHO 11 Symposium, Noordwijk, ed. A. Wilson, Netherlands, ESA SP-508, 303
Kopp, G., Lindsey, C., Roellig, T. L., et al. 1992, ApJ, 388, 203
Krijger, J. M., Rutten, R. J., Lites, B. W., et al. 2001, A&A, 379, 1052
Lites, B. W., Rutten, R. J., & Kalkofen, W. 1993, ApJ, 414, 345
Loukitcheva, M., Solanki, S. K., Carlsson, M., & Stein, R. F. 2004a, A&A, 419, 747
Loukitcheva, M., Solanki, S. K., & White, S. 2004b, in Multi-Wavelength Investigations of Solar Activity, ed. A. V. Stepanov, E. E. Benevolenskaya, & A. G. Kosovichev (Cambridge University Press), Proc. IAU Symp., 223, 643
Rutten, R. J., & Uitenbroek, H. 1991, Sol. Phys., 134, 15
Solanki, S. K. 2004, in Multi-Wavelength Investigations of Solar Activity, ed. A. V. Stepanov, E. E. Benevolenskaya, & A. G. Kosovichev (Cambridge University Press), Proc. of IAU Symp. 223, 195
Solanki, S. K., & Steiner, O. 1990, A&A, 234, 519
Torrence, C., & Compo, G. 1998, Bull. Am. Meteorol. Soc., 79, 61
Vernazza, J. E., Avrett, E. H., & Loeser, R. 1981, ApJS, 46, 635
White, S., Loukitcheva, M., & Solanki, S. K. 2006, A&A, 456, 697 (Paper I)
Wedemeyer, S., Freytag, B., Steffen, M., Ludwig, H.-G., & Holweger, H. 2004, A&A, 414, 1121
Wedemeyer-Böhm, S., Ludwig, H.-G., Steffen, M., Freytag, B., & Holweger, H. 2005a, Proc. 13th Cool Stars Workshop, ed. F. Favata et al., 1035
Wedemeyer-Böhm, S., Ludwig, H.-G., Steffen, M., Leenaarts, J., & Freytag, B. 2005b, A&A, in prep.
Wilhelm, S., & Kalkofen, M. 2003, A&A, 408, 1137